Novel Preparation Method of TiO_2-Nanorod-Based Photoelectrodes for Dye-Sensitized Solar Cells with Improved Light-Harvesting Efficiency

Luisa De Marco,[†] Michele Manca,*[,‡] Roberto Giannuzzi,[†] Francesco Malara,[†] Giovanna Melcarne,[†] Giuseppe Ciccarella,[†] Isabella Zama,[§] Roberto Cingolani,[‡] and Giuseppe Gigli[†,‡]

NNL, National Nanotechnology Laboratory of CNR-INFM c/o Istituto Superiore Universitario di Formazione Interdisciplinare, sez. Nanoscienze, Distretto Tecnologico, Università del Salento, Via Arnesano 16, Lecce 73100, Italy, IIT, Italian Institute of Technology, Energy Plattform, Via Morego 30, Genova 16163, Italy, and DSC, Daunia Solar Cell c/o TRE-Tozzi Renewable Energy Group, Via Zuccherificio 10, Mezzano (RA) 48100, Italy

Received: October 29, 2009; Revised Manuscript Received: December 20, 2009

We present a novel, facile, and cost-effective method to prepare highly transparent mesoporous films made by anatase TiO_2 nanorods that have been synthesized by a single-step solvothermal process. Such nanorods have been conveniently used as prepared—without completely removing the residual organics—to obtain suitable screen-printable paste by means of the use of proper polymeric binders. This method has been successfully implemented to fabricate highly efficient nanorod-based photoelectrodes for dye-sensitized solar cells. They showed an increment of the overall quantum conversion efficiency comprised between 34% and 58% with respect to cells based on commercial P25 titanium dioxide nanoparticles. In particular, a maximum photocurrent density and solar conversion efficiency of 16.9 mA/cm^2 and 7.9% have been obtained, respectively.

Introduction

In the past decade, nanostructured materials have received considerable attention due to their unique properties and the large range of novel applications in which they can be exploited.[1−10] Many efforts have been concentrated on a wide variety of metal oxides, such as TiO_2, SnO_2, VO_2, and ZnO. Among them, TiO_2 and TiO_2-derived materials have been extensively used for various applications, such as dye-sensitized solar cells (DSSC), water treatment, catalysts, gas sensors, etc.[11−19] In particular, solar cells based on dye sensitization of mesoporous TiO_2 electrodes are regarded as a low-cost and high-efficiency alternative to conventional photovoltaic devices.[4,10,12,13,18−26] DSSCs consist of a monolayer of a photosensitizing dye adsorbed on a mesoporous film of nanocrystalline oxide semiconductors, typically the anatase titanium dioxide. Dye molecules are chemisorbed through functional anchoring groups on the surface of the semiconductor, while the pores of the film are generally filled with an iodide/triiodide electrolyte. When an incident photon excites the dye, this injects an electron into the conduction band of the semiconductor. Positively charged dyes are then reduced by the iodide species I^-, and the electrical circuit is completed by the reduction of I_3^- at the platinum counter electrode.[20]

For an efficient working mechanism, a large surface area at the dye/TiO_2 semiconductor interface is necessary to achieve extended chemisorption of dye molecules, whereas a porous structure is required to improve the interaction of the electrolyte with the oxidized dye so as to induce an efficient regeneration of the dye. Moreover, TiO_2 mesoporous films have to be characterized by good adhesion to the conductive glass and absence of cracks as well as by the presence of good interconnections between nanosized titania nanoparticles. This avoids charge-carrier accumulation, allows for efficient electron flow, and, finally, assures current collection at the back contact of the photoelectrode.[23]

To achieve titanium dioxide films with specifically designed morphological features, several hydrothermal synthesis procedures have been proposed so far.[27−32] Nevertheless, the insufficient electron diffusion coefficient in traditional electrodes composed of nanometer-sized TiO_2 particles (i.e., several orders of magnitude smaller than those in bulk single crystal TiO_2) still represents a significant limiting factor in the perspective of further improvements of the power conversion efficiency.[33] As is well-known,[34,35] electron collection is determined by trapping/detrapping events along the site of the electron traps (defects, surface states, grain boundaries, self-trapping, etc.). This point has promoted intensive research toward photoanodes comprising one-dimensional nanocrystalline materials with enhanced electron transport properties due to the decreased number of intercrystalline contacts and stretched grown structures with specific directionality.[26,28,36−44]

Highly porous nanotextured oxide films have been fabricated by implementing rod-shaped titania nanocrystals (20−30 nm × 100−300 nm) that reached a power conversion efficiency of 7.1% and a photocurrent density of 13.4 mA/cm^2 with a single nanorod layer of 16 μm in thickness;[36] this good performance was achieved owing to the increased rate of electron transport resulting from the high crystalline anatase nanorods, whereas the extent of dye adsorption related to the light-harvesting yield is poor due to the relatively low specific surface area.

More recently, Kang et al.[37] demonstrated an improvement in the electron transport of a photoelectrode based on smaller nanorods (4 nm × 20 nm sized) in comparison to 6 nm sized nanoparticle-based films and reported an efficiency of 6.2% and

* To whom correspondence should be addressed. E-mail: michele.manca@iit.it.
[†] NNL c/o Istituto Superiore Universitario di Formazione Interdisciplinare, Università del Salento.
[‡] IIT.
[§] DSC c/o TRE-Tozzi Renewable Energy Group.

10.1021/jp910346d
Published on Web 02/12/2010

photocurrent density of 15.3 mA/cm^2 with a 7.1 μm thick photoelectrode.

These results demonstrate that, by properly tuning the size and the shape of nanoparticles, it is possible to fabricate photoelectrodes responding to both requirements of large surface area and efficient electron transfer.

On the basis of the tremendous advances achieved by colloidal chemistry in the last two decades, it is nowadays possible to obtain high-quality nanocrystals within a wide spectrum of sizes and shapes; in particular, the solvothermal methods have been largely employed to synthesize TiO_2 nanoparticles and nanorods, owing to the better control on crystallinity, size, and shape distributions of the nanocrystals with respect to the classical hydrothermal methods as well as to the possibility to synthesize easily redispersible titania nanoparticles.[45−48]

According to our knowledge, the synthetic methods that have been reported so far for the preparation of TiO_2 nanocrystals for dye-sensitized solar cells are based on hydrothermal processes.[4,12,13,19−21,23,27,32] In almost all of those reported cases, it is quite difficult to avoid the aggregation of synthesized nanoparticles that may induce inhomogeneity and lead to the presence of cracks in the sintered film. This dramatically affects the energy conversion efficiency of the DSSC.

Starting from these remarks, in the present paper, we propose a novel procedure for the synthesis of rod-shaped (5 nm × 30 nm sized) anatase TiO_2 nanocrystals by means of a one-step solvothermal approach (a modified benzyl alcohol route) and for their effective application in DSSCs by means of a suitable and easy to prepare screen-printable paste. The original dimensions of the nanorods are preserved in the sintered photoelectrode thanks to the abundant organic capping layer produced during the solvothermal synthesis. The presence of organic compounds on the surface of the nanoparticles prevents, in fact, coalescence phenomena from taking place during the subsequent phases of paste preparation and sintering process.

Such a procedure provides an innovative, facile, and cost-effective way to fabricate crack-free, highly transparent mesoporous titanium dioxide films capable of combining the good transport properties of one-dimensional nanocrystals with the huge surface area of the finely dispersed nanoparticles.

Experimental Section

Materials. Ti(IV) isopropoxide (Ti(OPri)$_4$ or TTIP, 97%), benzyl alcohol (BzOH, ≥99%), acetic acid (AcOH, 99.3%), polyethylene oxide (PEO, average M_w ~100 000), lithium iodide (99.9%), iodine (99.99%), 1-methyl-3-propylimidazolium iodide (≥98.0%), and 4-*tert*-butylpyridine (96%), were purchased from Aldrich. The reagents were employed as received without additional purification.

The epoxy resin (accuGen 100 Nd), 1,4-cyclohexanedimethanol diglycidyl ether in a solution of propylene carbonate containing the photoacid generator (mixed triarylsulfonium/hexafluoroantimonate salt), was provided by 3D Systems GmbH.

Transparent conductive oxide-coated glass TCO10−10, 1.1 mm thick 10 ohm/sq N719 dye, T-SP screen-printable paste, and Surlyn hot-melt polymer were provided by Solaronix S.A.

Synthesis of TiO_2 Nanocrystals and Paste Preparation. TiO_2 colloids were prepared according the following procedure: A 1 mL portion of TTIP (3.36 mmol) was added to 0.75 mL of AcOH (13 mmol) along with 4.25 mL of BzOH (TTIP/AcOH molar ratio = 1/4). The solution was stirred for 30 min at room temperature after which the reaction vessel was closed with a Teflon cap and kept to 150 °C per 8 h; during this time, the solution turns from clear to a milky suspension. The reaction was then stopped, and the suspension was centrifuged (6 000 rpm for 30 min). To obtain a screen-printable paste, 200 mg of polyethylene oxide, M_w ~100 000, was added to 1 g of the precipitate of the reaction (which contains an amount of titanium dioxide equal to 17%) and mixed well enough to obtain a homogeneous paste; epoxy resin (100 mg) was then added and mixed.

DSSC Fabrication. FTO glasses were cleaned in a detergent solution using an ultrasonic bath for 15 min, then washed with water and ethanol. The TiO_2 paste was deposited onto the conducting glass by screen-printing (screen characteristic: material, polyester; mesh count, 120 mesh/cm) and dried at 160 °C for 6 min; this procedure was repeated several times in order to obtain the wanted film thickness. The film thickness and the dimensions of the active area were measured using the profilometer. Both a P25-based paste prepared according the reported literature[25] and a commercial screen-printable paste, Solaronix T/SP (see the Supporting Information), were used to fabricate reference photoelectrodes with different thicknesses. All the films were characterized by the same value of active area (0.28 cm^2). The FTO glass samples coated with the TiO_2 pastes were gradually heated under an air flow at 160 °C for 20 min, at 325 °C for 5 min, at 375 °C for 5 min, at 450 °C for 15 min, and at 500 °C for 15 min. After cooling to 80 °C, the TiO_2 electrodes were immersed into a solution of 0.5 mM (bis(tetrabutylammonium)-*cis*-di(thiocyanato)-*N*,*N*′-bis (4-carboxylato-4′-carboxylic acid-2,2-bipyridine) ruthenium(II) (N719) in a mixture of acetonitrile and *tert*-butyl alcohol (v/v, 1:1) and kept at room temperature for 14 h.

The solar cells was assembled by placing a platinum-coated conducting glass (counter electrode) on the N719 dye-sensitized photoelectrode (working electrode). The two electrodes were assembled into a sandwich type cell and sealed with a Surlyn hot-melt gasket 30 μm thick. The redox electrolyte was introduced into the space of interelectrodes through the hole predrilled on the back of the counter electrode. The holes were sealed up using Surlyn hot-melt film and a cover glass. The redox electrolyte used was 0.1 M LiI, 0.05 M I_2, 0.6 M 1-methyl-3-propylimidazolium iodide, and 0.5 M *tert*-butylpyridine in dried acetonitrile.[23]

Characterization. The Ti atomic content of the nanocrystal slurry was measured by inductively coupled plasma atomic emission spectroscopy (ICP-AES) measurements with a Varian Vista AX spectrometer. The samples for analyses were digested in concentrated HF/HNO_3 (4/1, v/v).

Low-magnification TEM images of TiO_2 NRs were recorded with a JEOL JEM 1011 microscope operating at an accelerating voltage of 100 kV. The samples for TEM analyses were prepared by dropping a dilute solution of the NRs dissolved in chloroform onto carbon-coated copper grids and then allowing the solvent to evaporate.

The thickness of the transparent films was measured with a Tencor Alpha-Step 500 surface profiler. A Varian Cary 5000 UV−vis spectrophotometer was used to measure the UV−vis absorption spectra of the as-prepared films and the desorption solutions.

SEM characterization of TiO_2 photoelectrodes' morphology was performed with a RAITH 150 EBL instrument. Typically, the images were acquired at 5 kV accelerating voltages using short exposure times.

A SMENA MT-DTA atomic force microscope (AFM) in tapping mode was used for surface topographical characterization. All acquired AFM images were analyzed using the

detection software SPIP, and several statistic parameters were used to characterize the topography. Among these, the Wenzel coefficient R_f,[49] denoted as the ratio between the surface area (taking the z height into account) and the area of the flat xy plane, was calculated as

$$R_f = 1 + \frac{(\sum_{k=0}^{M-2}\sum_{l=0}^{N-2} A_{kl}) - (M-1)(N-1)\delta x\,\delta y}{(M-1)(N-1)\delta x\,\delta y} \quad (1)$$

where

$$A_{kl} = \frac{1}{4}\left|\sqrt{\delta y^2 + (z(x_k, y_l) - z(x_k, y_{l+1}))^2} + \sqrt{\delta y^2 + (z(x_{k+1}, y_l) - z(x_{k+1}, y_{l+1}))^2}\right| \cdot \left|\sqrt{\delta x^2 + (z(x_k, y_l) - z(x_{k+1}, y_l))^2} + \sqrt{\delta x^2 + (z(x_k, y_{l+1}) - z(x_{k+1}, y_{l+1}))^2}\right| \quad (2)$$

Photocurrent−voltage ($I-V$) measurements were performed using a Keithley unit (model 2400 Source Meter). A Newport AM 1.5 solar simulator (model 91160A, equipped with a 300 W xenon arc lamp) served as a light source, and its light intensity (or radiant power) was calibrated to 100 mW/cm^2 using a reference a Si solar cell. The light source for the incident photon-to-current conversion efficiency (IPCE) measurements was the solar simulator equipped with a Spectral Products monochromator (model CM110 1/8 m). The intensity was measured with a Newport radiant power meter (model 70260 combined with the 70268 Probe) and a UDT Instrument model 221 calibrated photodiode.

Three parallel samples for each kind of layer structure were made for $I-V$ and IPCE measurement, and the reproducibility of the TiO_2 photoelectrodes was quite good. Electrochemical impedance spectroscopy (EIS) spectra have been measured by using an AUTOLAB PGSTAT 100 potentiostat operating in two-electrode mode. Measurements have been carried out in the dark at a potential corresponding to the value of the open-circuit state under 1sun illumination, a frequency range of 300 kHz−30 mHz, and an ac voltage of 10 mV. The frequency-dependent impedance was fitted by using the EC-LAB software (from BioLOGIC).

Results and Discussion

Synthesis of TiO_2 Nanocrystals. Referring to the synthesis procedures of TiO_2 nanocrystals, it is well-known that sol−gel reactions allow good control in every single step, from the rate of hydrolysis of the molecular precursor to the definition of size and morphology of the final product.[45]

Most of these sol−gel methods are based on the aqueous hydrolysis of an alkoxide or halide precursor and subsequent condensation to the inorganic framework of the nanoparticle; although additives (such as tetramethylammonium hydroxide) or capping agents (such as cetyltrimethylammonium bromide, trioctylphosphine oxide, etc) have proven to be suitable instruments for control over particle size and shape, the fast hydrolysis and condensation rates remain a major problem, as well as particle agglomeration.

In the past decade, to overcome many of the specific problems for aqueous systems, nonhydrolytic sol−gel processes have been developed.[47,48,50−52]

Since 2002, Niederberger found that the reaction between benzyl alcohol and $TiCl_4$ could provide a versatile method for nonaqueous preparation of TiO_2 nanocrystals: 5 nm sized anatase nanoparticles were obtained by means of a synthesis performed at 40 °C for 7−14 days.[50,51]

Our synthetic approach[53] is indeed based on a modification of this known nonaqueous sol−gel process by the use of titanium tetraisopropoxide as titanium oxide precursor. The introduction of acetic acid in the synthesis (TTIP/acetic acid molar ratio = 1:4) is necessary to better control hydrolysis and condensation rates: actually, a modification of TTIP by acetic acid occurs in the early stage of the process, and so, through the formation of a stable complex, the availability of groups that could fast hydrolyze and condense is reduced.[54] Size and shape of the growing seeds are controlled by the coordinating action of the acetic acid that complexes them with the carboxylic ligands in the surface.[45]

A TEM image and the corresponding XRD spectrum of TiO_2 nanocrystals synthesized by the above-described procedure are reported in Figure 1. Rodlike nanoparticles having uniform lengths up to 30 nm and a diameter of 5 nm are clearly visible. A TEM image of commercial P25 nanoparticles is also reported as a comparison. The X-ray diffraction spectrum, compared with the well-known standard anatase pattern, shows that only the anatase phase is present.

It has been remarked that this method does not require water as solvent because the esterification reaction between the benzyl alcohol and the unreacted acetic acid gradually provides water into the reaction environment. It constitutes, then, a simple and relatively fast procedure for the preparation of TiO_2 anatase nanorods. It is particularly fit to be scaled-up on large volumes in the perspective of a potential industrialization.

Fabrication of TiO_2-Nanorod-Based Photoelectrodes. To obtain highly efficient photoelectrodes for DSSCs, TiO_2 nanorods prepared through the above-described procedure have to be turned into a thick mesoporous film capable of satisfying two basic requirements: (1) high surface area maximizing light absorption and (2) high effective diffusion coefficient allowing electrons to reach the TCO surface before charge recombination occurs.

The challenge was to preserve the original properties of the nanocrystals: rod shape and small dimension might be considered the most important parameters because they have a tremendous effect on transport properties and light harvesting.

The wet slurry obtained by removing the supernatant at the end of the solvothermal synthesis contained about a 17 wt %/wt of titanium dioxide nanocrystals (as revealed by ICP-AES analysis), while the remaining 83 wt %/wt was constituted by organic compounds (mainly benzyl alcohol, benzyl acetate, and acetic acid), both chemically adsorbed and/or physically adsorbed onto the nanorods surface.

According to our approach, the organics employed in the synthesis play a pivotal role in maintaining good nanoparticle dispersion also after the end of the synthetic procedure. They act, in fact, as a "soft template" that keeps the nanoparticles well-separated and, at the same time, is fundamental for the formation of a mesoporous structure during the subsequent sintering step.

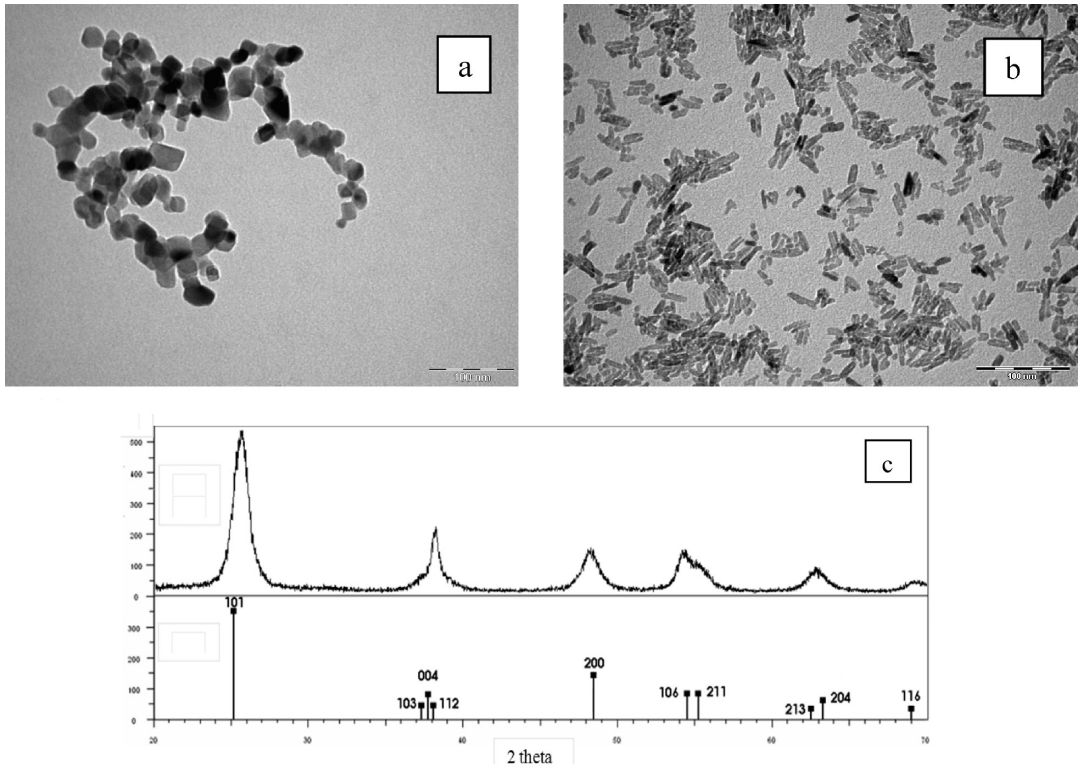

Figure 1. TEM images of P25 commercial nanoparticles (a) and of rod-shaped TiO_2 nanocrystals synthesized by means of the solvothermal route (b). (c) XRD spectrum of such nanocrystals.

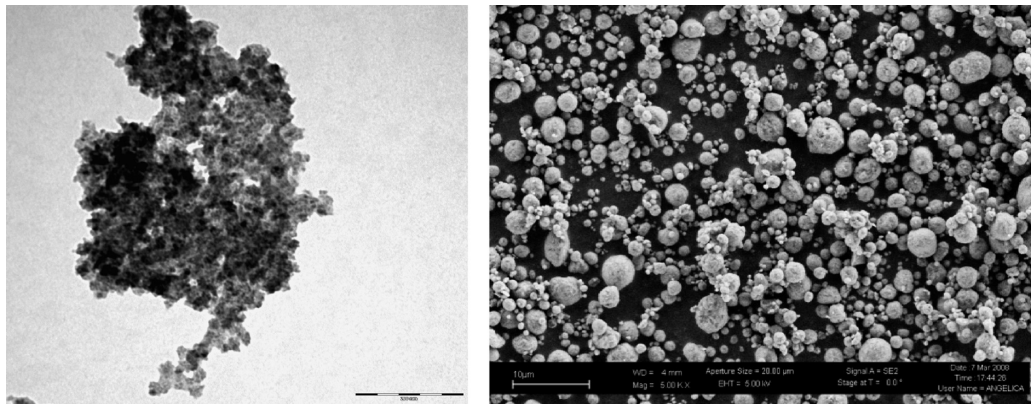

Figure 2. TEM and SEM images of aggregated TiO_2 nanocrystals obtained by spray-drying.

On the other hand, it makes it difficult to remove the capping layer by any washing (with ethanol or isopropyl alcohol) or drying procedure; rather, these treatments promote nanocrystal coalescence.

We observed, in fact, that, when dried or spray-dried, nanocrystals lose their original morphology and form micrometer-sized aggregates that are no more separable by conventional milling techniques. In Figure 2, we reported both a TEM and an SEM image showing the typical morphology of nonhydrolytically synthesized titanium dioxide powder as obtained by the spray-drying process.

Such aggregation phenomena have the effect of reducing the surface area, thus the light-harvesting capability of the photoelectrode,[42] as well as to induce the formation of cracks during the sintering process.

The reaction product was conveniently used as prepared, without completely removing the residual organic compounds. After the supernatant was eliminated by centrifugation, the precipitate was directly mixed with proper polymeric binders. The choice of additives that can properly interact both with the capped nanoparticles and with the FTO-coated substrate is crucial to the aim of producing well-adherent and crack-free mesoporous films. To this purpose, several paste formulations have been designed and tested by implementing well-known paste preparation methods.[19−25,29−32,36,37]

The best outcome in terms of processability and photoelectrode performances has been achieved with a paste having the following chemical composition: TiO_2 nanorods, 13 wt %/wt; synthesis organic residuals, 64 wt %/wt; polyethylenoxide (100 000 M_w), 15 wt %/wt; epoxy resin (accuGen 100 Nd), 8 wt %/wt.

This method was particularly effective because it avoids the step of nanocrystal dispersion and, at the same time, served to maintain their primitive morphology. Moreover, by a single deposition and sintering process, it was also possible to obtain photoelectrodes thicker than 4 μm, unlike what is reported about the preparation of other nanorod-based photoelectrodes, where repeated sintering processes are required.[28,36,55]

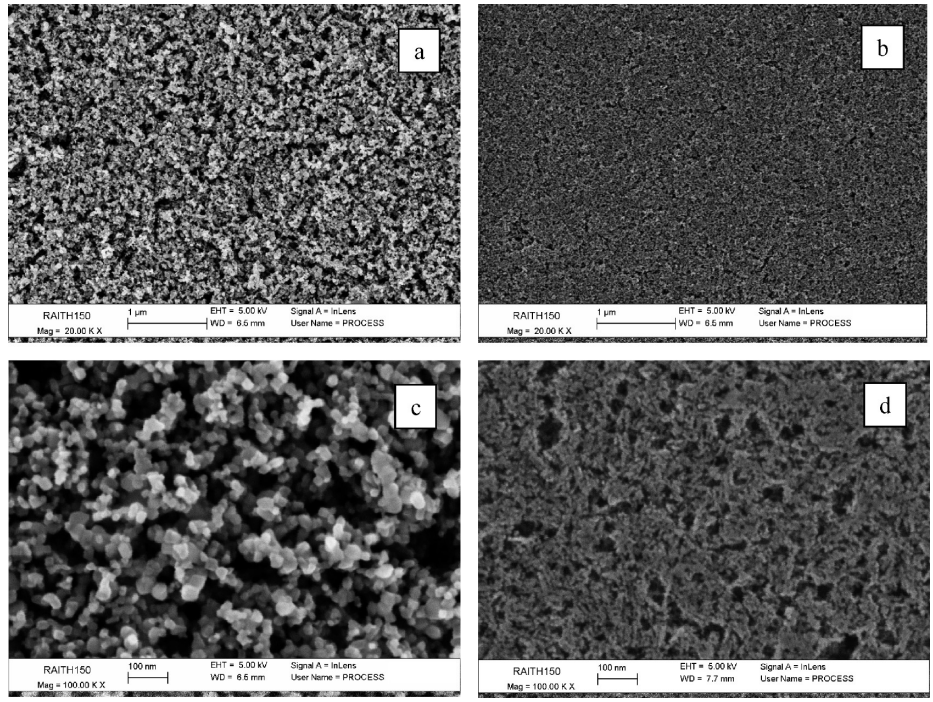

Figure 3. SEM images showing the morphology of the sintered films: (a, c) a photoelectrode obtained by a P25-based paste and (b, d) a photoelectrode obtained by an ST-NR-based paste.

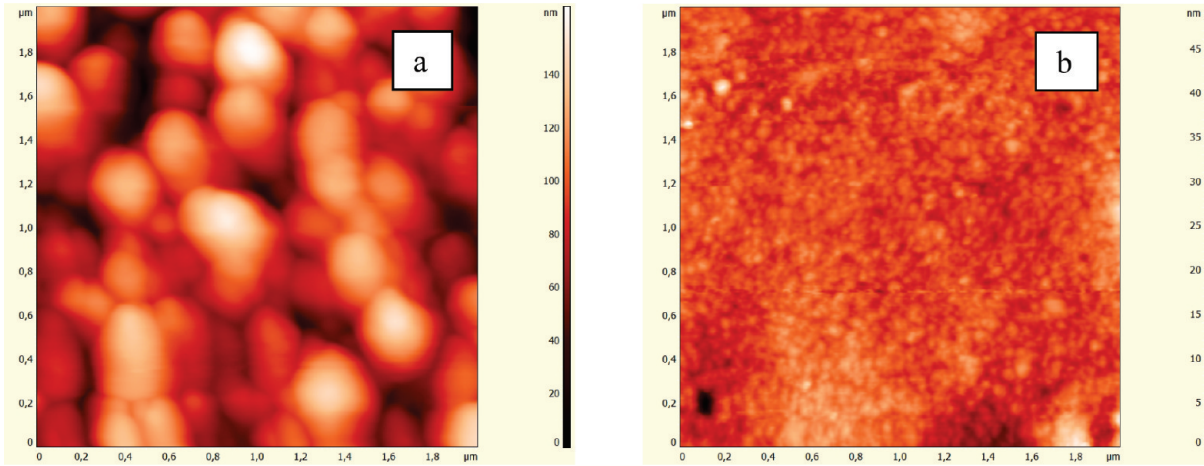

Figure 4. AFM images of a P25-based (a) and of an ST-NR-based (b) photoelectrode.

To estimate the performance of photoelectrodes based on our synthesized titania nanorods, several photoelectrodes made by P25 titania nanoparticles as well as by commercial Solaronix T/SP paste (see the Supporting Information) were fabricated as references.

In Figure 3, we report the SEM micrographs of both the films. As it can be clearly noticed, films prepared with P25-based paste had a coarse nanotexture with small (20 nm) and large (50 nm) roughly interconnected nanoparticles. Solvothermal synthesized nanorods (ST-NRs) showed, instead, the formation of a continuous highly porous three-dimensional network with typical "spongy" structures that are tightly linked to the FTO/glass substrate.

The mean width of nanocrystallites in the film is determined by the size of the synthesized nanorods, and no clear change can be observed in their dimension. These results indicated that the organic capping layer effectively kept the nanoparticles well-separated even at high sintering temperature, protecting their original morphology (unlike what happens with the dried powder); moreover, such a paste preparation method maintained the homogeneity in the film and also avoided formation of aggregates and cracks.

In addition, the burning and decomposition of the organics during the calcination process turned the film into a highly porous structure that is also characterized by the presence of larger cavities that can enhance the penetrability of the dye solution during the uptaking process, as well as the electrolyte diffusion during the cell operation.

To better reveal the increase in the surface area, an AFM characterization has also been performed (see Figure 4). rms roughness and Wenzel coefficient R_f—denoted as the ratio between the surface area (taking the z height into account) and the area of the flat xy plane—were extrapolated by using the detection software SPIP.[56]

ST-NR-based photoelectrodes showed an average rms value of ~83 nm for a 20 × 20 μm^2 scanned area, whereas values in the range between 51 and 55 nm were detected from the P25-based photoelectrode analysis. Besides this, an increment of

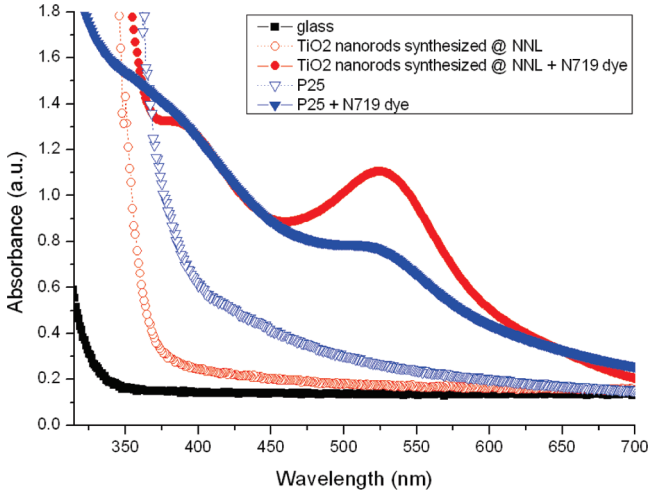

Figure 5. Absorption spectra of 4 μm thick P25- and ST-NR-based photoelectrodes before and after the dye uptaking process.

more than 40% of the Wenzel coefficient—that is, an expression of the topographic surface area—was found in the case of nanorods (2.03 vs 1.44).

As result of the higher surface area, a higher number of dye molecules are adsorbed onto the TiO_2-nanorod-based photoelectrode, as shown by absorbance measurements. In Figure 5, we report the absorption spectra of 4 μm thick P25- and ST-NR-based photoelectrodes before and after the dye uptaking process.

The increased transparency in the visible light range of the ST-NRs film—due to the minimization of the light-scattering phenomena—determines a higher absorption once the TiO_2 layer is dye-sensitized. This light-harvesting capability improvement can be clearly noticed by comparing the absorption spectra of both photoelectrodes sensitized by N719. In particular, ST-NR-based photoelectrodes show an enhancement of absorption intensity peak of a factor of 1.55 with respect to the reference P25 sample.

To determine the exact amount of uptaken dye molecules, the sensitized photoelectrodes (4 μm thick) were separately immersed for 8 h at room temperature into a vessel containing 5 mL of 0.1 M NaOH water/ethanol (1:1, v/v) solution, in order to allow a full dye desorption. We calculated the amount of dye loaded on both photoelectrodes from the absorption measurements of such solutions by considering $\varepsilon = 1.41 \times 10^4$ M^{-1} cm^{-1} as the molar extinction coefficient for N719 at 515 nm.[23] A value of 1.45×10^{-8} mol/cm^2 of N719 molecules was adsorbed by the ST-NR-based film, more than twice the amount of dye (0.55×10^{-8} mol/cm^2) adsorbed onto the P25-based photoelectrode.

Application to DSSCs

The efficiency (η %), fill factor (FF), open-circuit voltage (V_{oc}), and short-circuit current density (J_{sc}) of DSSCs with different thicknesses of both P25- and ST-NR-based photoelectrodes are reported in Table I, which shows the dependence of the light-to-electricity conversion efficiencies on the thickness of TiO_2 films.

As a consequence of the higher surface area, photoelectrodes based on TiO_2 nanorods synthesized by the solvothermal route produced higher photocurrents than the corresponding photoelectrodes made by commercial titania nanoparticles. For relatively thin photoelectrodes (4−6 μm), ST-NR-based DSSCs generate almost double the photocurrent densities in comparison with P25-based ones, thus attesting to the larger amount of dye that can be uptaken on ST-NR mesoporous films, as discussed above. Such a difference tends to decrease for thicker photoelectrodes as the overall absorbing surface approaches the value corresponding to the total extinction length of the incident light. This value depends, as is well-known, on the extinction coefficient of the adsorbed dye and on the morphological characteristics of the single nanoparticles constituting the film: the TiO_2 particles prepared in this work are much smaller than commercial P25 and, most of all, maintain their small dimension in the sintered film, so in our DSC, the TiO_2 can adsorb more dye than that produced with larger sized particles with the same film thickness; this latter is the reason why, for example, an only 8 μm thick ST-NR-based photolectrode is capable of generating the same photocurrent density (about 11.2 mA/cm^2) as a 14 μm thick P25-based photoelectrode.

On the other hand, the V_{oc} slightly decreases for thicker mesoporous films, where charge recombination and electron transport limitations become more significant because of the longer path of injected electrons across colloidal particles and grain boundaries. In addition, in ST-NRs cells, an average reduction of the open-circuit voltage is observed with respect to P25 cells; this is probably a secondary effect of the finer morphology structure associated with the larger number of nanoparticle interconnections, which provides additional charge-recombination sites. As a result, ST-NR-based cells show an increment of the overall quantum conversion efficiency η comprised between 34% and 58% compared to P25-based ones. In particular, with a 14 μm thick ST-NR photoelectrode, DSSCs generating a 16.9 mA/cm^2 photocurrent density with a conversion efficiency of 7.9% have been realized.

Figure 6 displays the incident monochromatic photon-to-current conversion efficiency (IPCE) at short-circuit conditions of 14 μm thick both P25- and ST-NR-based cells, as a function of wavelength. Maximum IPCE values of 82% and 55% are obtained at 530 nm for the ST-NR and P25 cells, respectively. This increase is in good agreement with the measured enhancement of J_{sc} and the dye uploading values.

It has been, however, remarked that the above-described procedure allows one to obtain more than 10 μm thick photoelectrodes still showing a good transparency, but this does not necessarily represent the optimized condition in terms of DSSC performances. It is well-known, in fact, that adding a scattering layer on the top of the working electrode, which can properly reflect the unused portion of incident light, is a common way to maximize the DSSCs' efficiency. The addition of a

TABLE I: Dependency of Efficiency, Photocurrent Density, Photovoltage, and Fill Factor on the Thickness of the Film

thickness [μm]	P25 η %	ST-NR η %	P25 V_{oc} [V]	ST-NR V_{oc} [V]	P25 J_{sc} [mA/cm^2]	ST-NR J_{sc} [mA/cm^2]	P25 FF	ST-NR FF
4	**2.4**	**3.8**	0.75	0.71	4.7	7.8	0.69	0.69
6	**2.9**	**4.7**	0.73	0.69	6.0	10.1	0.69	0.68
8	**3.7**	**5.2**	0.73	0.68	7.2	11.2	0.70	0.68
10	**4.2**	**6.3**	0.71	0.68	8.5	13.7	0.70	0.68
14	**5.5**	**7.9**	0.70	0.68	11.3	16.9	0.70	0.69

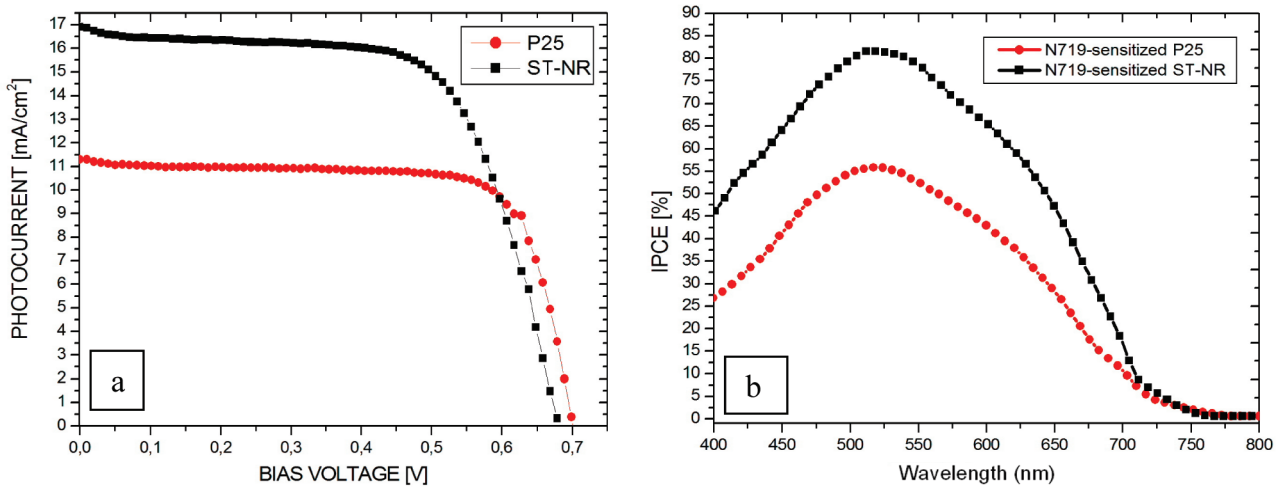

Figure 6. $I-V$ characteristics (a) and IPCE spectra (b) of DSSCs having a 14 μm thick P25- (circles) and ST-NR-based (squares) photoelectrode.

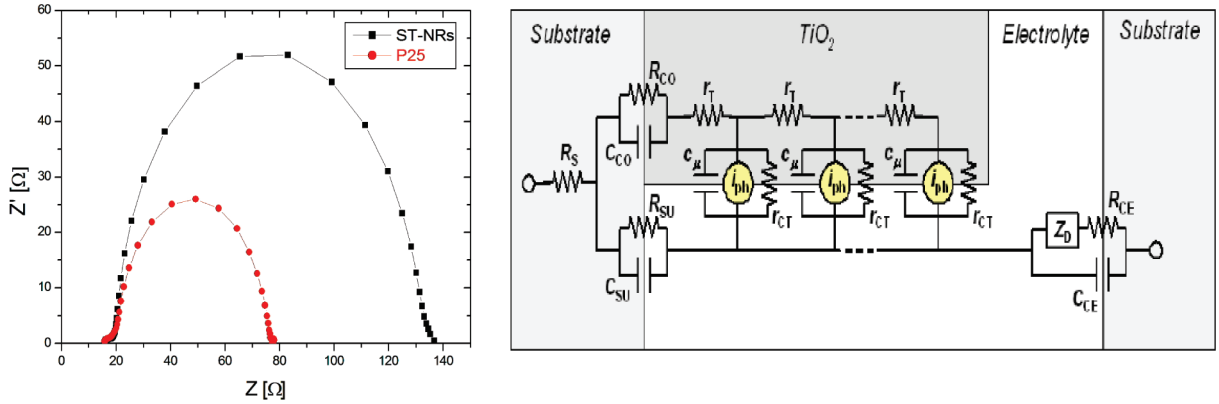

Figure 7. (a) Electrochemical impedance spectra of DSSCs made with ST-NR- and P25-based photoelectrodes. (b) General equivalent circuit model of a DSSC.[59] The r_{CT} is the charge-transfer resistance of the charge-recombination process between photogenerated electrons and I_3^- in the electrolyte; c_μ is the chemical capacitance of TiO_2 film; Z_D is the Warburg element showing the Nernst diffusion of I_3^- in the electrolyte; R_{CE} and C_{CE} are the charge-transfer resistance and double-layer capacitance at the counter electrode (platinized TCO glass); R_{SU} and C_{SU} are the charge-transfer resistance and the corresponding double-layer capacitance at the exposed TCO/electrolyte interface; R_{CO} and C_{CO} are the resistance and the capacitance at the TCO/TiO_2 contact; and R_s is the series resistance, including the sheet resistance of TCO glass and the contact resistance of the cell.

scattering layer to our ST-NR-based photoelectrodes is expected to produce a further enhancement of the DSSC performances.

Finally, to highlight the differences in terms of charge-transfer phenomena between our nanorods and the commercial nanoparticles, an electrochemical characterization of the cells has been performed. Electrochemical impedance spectroscopy (EIS) is the most effective technique to investigate the charge-transport phenomena in a DSSC.[57] Figure 7 shows the EIS spectra measured in the dark at a potential corresponding to the value of the open-circuit state under 1sun illumination and plotted in a Nyquist diagram for a frequency range comprised between 30 mHz and 100 kHz for 10 μm thick photoelectrode-based cells. At such conditions, there were only two arcs detectable. The main contribution to the first (high-frequency) arc arises from the parallel connection of the coupling between the Helmholtz capacities of both electrodes and the charge-transfer resistance at the FTO/photoelectrode interface.[58] The charge-transfer resistance of the platinized FTO counter electrode is considered to be relatively small as it presents little changes with potential in comparison with bare FTO. The second (intermediate frequency) arc corresponds to electron-transfer resistance from the dye-sensitized nanocrystalline TiO_2 film to the electrolyte as well as to the back reaction of electrons with I_3^- via the FTO. The third (low frequency) arc—corresponding to the diffusion of I_3^- (holes) in the electrolyte—has not been detected here.

For fitting the experimental data, the equivalent circuit proposed by Wang et al.[60] for cells exhibiting a good carrier collection efficiency was used. Constant phase elements have been used instead of pure capacitors as they better describe the uneven and porous electrodes. In Table II, we report the extrapolated values for the following parameters:

- series charge-transfer resistance, $R_{CO} + R_{CE}$.

- series double-layer capacitance, $C_{CO}//C_{CE}$, and its correspondent capacitor ideality's coefficient, $a_{CO//CE}$.

- transfer resistance of the charge-recombination processes at the titania/dye/electrolyte interface, R_{CT}.

- electron transport resistance within the mesoporous photoelectrode, R_t.

- chemical capacitance of the charge-recombination processes at the titania/dye/electrolyte interface, C_{CT}, and its capacitor ideality's coefficient, a_{CT}.

Passing from the P25-based photolectrode to the ST-NR-based one, the charge-transfer resistance, $R_{CO} + R_{CE}$, slightly decreases from 8.2 to 5.1 Ω as a consequence of an improvement in the electrical contact with FTO mostly arising from the better adherence of the ST-NR-based film. As a secondary

TABLE II: Fitted Parameters from the Wang[60] Equivalent Circuit

cell	$R_{CO} + R_{CE}$ [Ω]	$C_{CO}//C_{CE}$ [mF]	a_{CO+CE}	R_{CT} [Ω]	R_t [Ω]	C_{CT} [μF]	a_{CT}
P25	8.2	3.72	0.40	58	51	380	1
ST-NRs	5.1	2.18	0.41	111	63	483	0.96

effect, it also exhibits a remarkably less intense capacitive behavior with respect to the P25-based cell, attesting to a reduction in the charge accumulation at the FTO/photoelectrode interface.

Concerning the second semicircle, a strong enhancement of the charge-transfer resistance in the intermediate frequency range was also observed for the cell made with the ST-NR-based photoelectrode: that value, in fact, almost doubled (111 vs 58 Ω) with respect to the case of the P25-based photoelectrode. This effect is, in part, associated with the larger number of interconnections existing between the nanorods—that implies a relatively higher electron diffusion impedance—but it is prevalently related to a consistent raising of the energy barrier to the spontaneous interfacial redox reactions involving the photogenerated electrons.

The main circuital elements that have been analyzed are the electron-transport resistance, R_t, within TiO_2—and, more specifically, the ratio between R_{CT} and R_t—and the chemical capacitance of the photoelectrode, C_{CT}. In terms of absolute values, the nanorod-based photolectrode shows a transport resistance of 63 Ω that is slightly higher with respect to the value corresponding to P25 (51 Ω). It has to be put in evidence that the absolute values of R_t cannot be compared because R_t is an extensive parameter that is thus related to the overall surface area of the photoelectrode and, as it has been demonstrated before, the surface area of nanorods is dramatically larger with respect to the commercial nanoparticles. What possesses a relevant physical meaning is, instead, the value of the ratio R_{CT}/R_t that really attests to a conspicuous improvement in electron collection efficiency associated with the rod-shaped nanocrystals.[61] The effective diffusion length within the mesoporous photoelectrode can be, in fact, deduced by the following equation[62]

$$L_e = d(R_{CT}/R_t)^{1/2} \quad (3)$$

where d is the thickness of the photoelectrode.

From the analysis of fitted data, a more than 30% increase in the electron diffusion length was revealed for the ST-NR-based photoelectrode.

A further confirmation of its more favorable property for electron transport was furnished by the calculation of the electron lifetime τ_e by means of the following relationship:

$$\tau_e = (C_{CT}R_{CT})^{1/a} \quad (4)$$

An electron lifetime of 46 ms for the ST-NR-based film was found against a value of 22 ms for the P25-based one.

Conclusions

In summary, we reported the synthesis of rod-shaped TiO_2 anatase nanocrystals by a simple one-step solvothermal method and their successful application as photoelectrodes for dye-sensitized solar cells through the preparation of a suitable screen-printable paste. The solvothermal approach prevented the formation of coarse aggregates and provided nanostructured films in which the original shapes and sizes of the constituting nanorods were preserved. Such prepared photoelectrodes showed a higher surface area and a better transparency with respect to commercial P25 titanium dioxide nanocrystal-based ones. The corresponding DSSCs resulted in an enhancement of the overall quantum conversion efficiency comprised between 34% and 58%. In particular, with a 14 μm thick photoelectrode, devices generating a 16.9 mA/cm^2 photocurrent density with a conversion efficiency of 7.9% have been realized. It is envisaged that, because of the simplicity and effectiveness of this procedure, it can be employed in a wide variety of large-scale both industrial and scientific applications.

Acknowledgment. This work has been partially supported by Daunia Solar Cell c/o TRE-Tozzi Renewable Energy group as an industrial partner. The authors thank Sonia Carallo for the AFM images; Paola Pareo for the SEM images; Benedetta Antonazzo for the TEM images; and Francesco Matteucci, Valerio Borzatta, Francesca Martina, Silvio Pappadà (Cuscinuma Sape), and Fabio Morrison for beneficial discussions.

Supporting Information Available: TEM images of TiO_2 nanoparticles from Solaronix T/SP paste, P25, and rod-shaped TiO_2 nanocrystals synthesized by means of the solvothermal route; SEM images showing the morphology of sintered P25, Solaronix, and nanorod-based photoelectrodes; absorption spectra of 4 μm thick P25-, Solaronix T-SP-, and ST-NR-based photoelectrodes before and after the dye uptaking process; table of values showing dependences of efficiency, photocurrent density, photovoltage, and fill factor on the photoelectrode's thickness of Solaronix T/SP- and ST-NR-based devices; electrochemical impedance spectra of dye solar cells made with ST-NR-, P25-, and Solaronix T/SP-based photoelectrodes (thickness = 10 μm); and table reporting values of the cell parameters determined by fitting the experimental data by means of the Wang[60] equivalent circuit. This material is available free of charge via the Internet at http://pubs.acs.org.

References and Notes

(1) Fujihira, M.; Satoh, Y.; Osa, T. *Nature* **1981**, *293*, 206.
(2) Wang, R.; Hashimoto, K.; Fujishima, A.; Chikuni, M.; Kojima, E.; Kitamura, A.; Shimohigoshi, M.; Watanabe, T. *Nature* **1997**, *388*, 431.
(3) Fujishima, A.; Rao, T. N.; Tryk, D. A. *J. Photochem. Photobiol., C* **2000**, *1*, 1.
(4) O'Regan, B.; Grätzel, M. *Nature* **1991**, *353*, 737.
(5) Rao, C. N. R.; Nath, M. *Dalton Trans.* **2003**, *1*, 1.
(6) Patzke, G. R.; Krumeich, F.; Nesper, R. *Angew. Chem., Int. Ed.* **2002**, *41*, 2446.
(7) Huang, M.; Mao, S.; Feick, H.; Yan, H.; Wu, Y.; Kind, H.; Weber, E.; Russo, R.; Yang, P. *Science* **2001**, *292*, 1897.
(8) Pan, Z. W.; Dai, Z. R.; Wang, Z. L. *Science* **2001**, *291*, 1947.
(9) Liu, Z.; Zhang, X.; Nishimoto, S.; Jin, M.; Tryk, D. A.; Murakami, T.; Fujishima, A. *Langmuir* **2007**, *23*, 10916.
(10) Wei, Q.; Hirota, K.; Tajima, K.; Hashimoto, K. *Chem. Mater.* **2006**, *18*, 5080.
(11) Adachi, M.; Murata, Y.; Harada, M.; Yoshikawa, S. *Chem. Lett.* **2000**, *8*, 942.
(12) Tan, B.; Wu, Y. *J. Phys. Chem. B* **2006**, *110*, 15932.
(13) Liu, B.; Aydil, E. S. *J. Am. Chem. Soc.* **2009**, *131*, 3985.
(14) Pavasupree, S.; Suzuki, Y.; Kitiyanan, A.; Pivsa-Art, S.; Yoshikawa, S. *J. Solid State Chem.* **2005**, *178*, 2152.
(15) Pavasupree, S.; Suzuki, Y.; Pivsa-Art, S.; Yoshikawa, S. *Sci. Technol. Adv. Mater.* **2005**, *6*, 224.
(16) Sasaki, T.; Nakano, S.; Yamauchi, S.; Watanabe, M. *Chem. Mater.* **1997**, *9*, 602.
(17) Cheng, B.; Russell, J. M.; Shi, W.; Zhang, L.; Samulski, E. T. *J. Am. Chem. Soc.* **2004**, *126*, 5972.
(18) Bacsa, R. R.; Dexpert-Ghys, J.; Verelst, M.; Falqui, A.; Machado, B.; Bacsa, W. S.; Chen, P.; Zakeeruddin, S. M.; Grätzel, M.; Serp, P. *Adv. Funct. Mater.* **2009**, *19*, 875.

(19) Nazzerruddin, M. K.; Kay, A.; Rodicio, I.; Humphy-Baker, R.; Muller, E.; Liska, P.; Vlachopoulos, N.; Grätzel, M. *J. Am. Chem. Soc.* **1993**, *115*, 6382.
(20) Kalyanasundaram, K.; Grätzel, M. *Coord. Chem. Rev.* **1998**, *77*, 347.
(21) Bach, U.; Lupo, D.; Comte, P.; Moser, J. E.; Weissörtel, F.; Salbeck, J.; Spreitzer, H.; Grätzel, M. *Nature* **1998**, *395*, 583.
(22) Kambe, S.; Murakoshi, K.; Kitamura, T.; Wada, Y.; Yanagida, S.; Kominami, H.; Kera, Y. *Sol. Energy Mater. Sol. Cells* **2000**, *61*, 427.
(23) Wang, Z. S.; Kawauchi, H.; Kashima, T.; Arakawa, H. *Coord. Chem. Rev.* **2004**, *248*, 1381.
(24) Tsoukleris, D. S.; Arabatzis, I. M.; Chatzivasiloglou, E.; Kontos, A. I.; Belessi, V.; Bernard, M. C.; Falaras, P. *Sol. Energy* **2005**, *79*, 422.
(25) Ito, S.; Chen, P.; Comte, P.; Nazzeruddin, M. K.; Liska, P.; Pechy, P.; Grätzel, M. *Prog. Photovoltaics* **2007**, *15*, 603.
(26) Grimes, C. A. *J. Mater. Chem.* **2007**, *17*, 1451.
(27) Barbé, C. J.; Arendse, F.; Comte, P.; Jirousek, M.; Lenzmann, F.; Shklover, V.; Grätzel, M. *J. Am. Ceram. Soc.* **1997**, *80*, 3157.
(28) Adachi, M.; Murata, Y.; Takao, J.; Jiu, J.; Sakamoto, M.; Wang, F. *J. Am. Chem. Soc.* **2004**, *126*, 14943.
(29) Kim, Y. J.; Lee, M. H.; Kim, H. J.; Lim, G.; Choi, Y. S.; Park, N. G.; Kim, K.; Lee, W. I. *Adv. Mater.* **2009**, *21*, 3668.
(30) Chen, D.; Huang, F.; Cheng, Y. B.; Caruso, R. A. *Adv. Mater.* **2009**, *21*, 2206.
(31) Yang, L.; Lin, Y.; Jia, J.; Xiao, X.; Li, X.; Zhou, X. *J. Power Sources* **2008**, *182*, 370.
(32) Gao, F.; Wang, Y.; Shi, D.; Zhang, J.; Wang, M.; Jing, X.; Humphry-Baker, R.; Wang, P.; Zakeeruddin, S. M.; Grätzel, M. *J. Am. Ceram. Soc.* **2008**, *130*, 10720.
(33) Enright, B.; Fitzmaurice, D. *J. Phys. Chem.* **1996**, *100*, 1027.
(34) Kopidakis, N.; Benkstein, K. D.; Van De Lagemaat, J.; Frank, A. J. *J. Phys. Chem. B* **2003**, *107*, 11307.
(35) Solbrand, A.; Henningsson, A.; Södergren, S.; Lindström, H.; Hagfeldt, A.; Lindquist, S. E. *J. Phys. Chem. B* **1999**, *103*, 1078.
(36) Jiu, J.; Isoda, S.; Wang, F.; Adachi, M. *J. Phys. Chem. B* **2006**, *110*, 2087.
(37) Kang, S. H.; Choi, S. H.; Kang, M. S.; Kim, J. Y.; Kim, H. S.; Hyeon, T.; Sung, Y. E. *Adv. Mater.* **2008**, *20*, 54.
(38) Law, M.; Greene, L. E.; Johnson, J. C.; Saykally, R.; Yang, P. D. *Nat. Mater.* **2005**, *4*, 455.
(39) Zhu, K.; Neale, N. R.; Miedaner, A.; Frank, A. J. *Nano Lett.* **2007**, *7*, 69.
(40) Mor, G. K.; Varghese, O. K.; Paulose, M.; Shankar, K.; Grimes, C. *Sol. Energy Mater. Sol. Cells* **2006**, *90*, 2011.
(41) Baxter, J. B.; Aydil, E. S. *Appl. Phys. Lett.* **2005**, *86*, 053114.
(42) Koo, B.; Park, J.; Kim, Y.; Choi, S. H.; Sung, Y. E.; Hyeon, T. *J. Phys. Chem. B* **2006**, *110*, 24318.
(43) Yang, W.; Wan, F.; Wang, Y.; Jiang, C. *Appl. Phys. Lett.* **2009**, *95*, 133121.
(44) Qu, J.; Gao, X. P.; Li, G. R.; Jiang, Q. W.; Yan, T. Y. *J. Phys. Chem. C* **2009**, *113*, 3359.
(45) Chen, X.; Mao, S. S. *Chem. Rev.* **2007**, *107*, 2891.
(46) Kim, C. S.; Moon, B. K.; Park, J. H.; Chung, S. T.; Son, S. M. *J. Cryst. Growth* **2003**, *254*, 405.
(47) Li, X. L.; Peng, Q.; Yi, J. X.; Wang, X.; Li, Y. D. *Chem.—Eur. J.* **2006**, *12*, 2383.
(48) Cozzoli, P. D.; Kornowski, A.; Weller, H. *J. Am. Chem. Soc.* **2003**, *125*, 14539.
(49) Wenzel, R. N. *Ind. Eng. Chem.* **1936**, *28*, 988.
(50) Niederberger, M.; Bartl, M. H.; Stucky, G. D. *Chem. Mater.* **2002**, *14*, 4364.
(51) Niederberger, M.; Bartl, M. H.; Stucky, G. D. *J. Am. Chem. Soc.* **2002**, *124*, 13642.
(52) Niederberger, M.; Garnweitner, G.; Krumeich, F.; Nesper, R.; Cölfen, H.; Antonietti, M. *Chem. Mater.* **2004**, *16*, 1202.
(53) Ciccarella, G.; Cingolani, R.; De Marco, L.; Gigli, G.; Melcarne, G.; Martina, F.; Matteucci, F.; Spadavecchia, J. World Patent 2009/101640 A1.
(54) Parra, R.; Góes, M. S.; Castro, M. S.; Longo, E.; Bueno, P. R.; Varela, J. A. *Chem. Mater.* **2008**, *20*, 143.
(55) Jiu, J.; Wang, F.; Sakamoto, M.; Takao, J.; Adachi, M. *J. Electrochem. Soc.* **2004**, *151*, A1653.
(56) *Scanning Probe Image Processor SPIP*; Image Metrology A/S: Hørsholm, Denmark, 2002.
(57) Fabregat-Santiago, F.; Bisquert, J.; Garcia-Belmonte, G.; Boschloo, G.; Hagfeldt, A. *Sol. Energy Mater. Sol. Cells* **2005**, *87*, 117.
(58) Hoshikawa, T.; Yamada, M.; Kikuchi, R.; Eguchi, K. *J. Electrochem. Soc.* **2005**, *152*, E68.
(59) Fabregat-Santiago, F.; Bisquert, J.; Palomares, E.; Otero, L.; Kuang, D.; Zakeeruddin, S. M.; Grätzel, M. *J. Phys. Chem. C* **2007**, *111*, 6550.
(60) Wang, Q.; Moser, J. E.; Grätzel, M. *J. Phys. Chem. B* **2005**, *109*, 14945.
(61) Wang, Q.; Ito, S.; Grätzel, M.; Fabregat-Santiago, F.; Mora-Serò, I.; Bisquert, J.; Bessho, T.; Imai, H. *J. Phys. Chem. B* **2006**, *110*, 25210.
(62) Wang, H.; Peter, L. M. *J. Phys. Chem. C* **2009**, *113*, 18125.

JP910346D